Accepted Article

Highly bright and stable lead-free double perovskite white light-emitting diodes

Shilin Jin, He Yuan, Tao Pang, Manjia Zhang, Junyang Li, Yuanhui Zheng, Tianmin Wu, Ruidan Zhang, Zhibin Wang, Daqin Chen *

S. L. Jin, H. Yuan, M. J. Zhang, J. Y. Li, Dr. R. D. Zhang, Dr. Z. B. Wang, Prof. D. Q. Chen

College of Physics and Energy, Fujian Normal University, Fuzhou, Fujian 350117, P. R. China

E-mail: dqchen@fjnu.edu.cn (D. Q. Chen)

Dr. T. Pang

Huzhou Key Laboratory of Materials for Energy Conversion and Storage, College of Science, Huzhou University, Zhejiang, Huzhou 313000, China

Prof. Y. H. Zheng, Prof. D. Q. Chen

Fujian Science & Technology Innovation Laboratory for Optoelectronic Information, Fuzhou, Fujian 350116, P. R. China

Prof. Y. H. Zheng

This article has been accepted for publication and undergone full peer review but has not been through the copyediting, typesetting, pagination and proofreading process, which may lead to differences between this version and the Version of Record. Please cite this article as doi: 10.1002/adma.202308487.

This article is protected by copyright. All rights reserved.

Accepted Article

College of Chemistry, Fuzhou University, Fuzhou, Fujian 350116, P. R. China

Prof. T. M. Wu

Key Laboratory of Opto-Electronic Science and Technology for Medicine of Ministry of Education, College of Photonic and Electronic Engineering, Fujian Normal University, Fuzhou, Fujian, 350117, China

Prof. D. Q. Chen

Fujian Provincial Collaborative Innovation Center for Advanced High-Field Superconducting Materials and Engineering, Fujian Normal University, Fuzhou, Fujian 350117, P. R. China

Prof. D. Q. Chen

Fujian Provincial Engineering Technology Research Center of Solar Energy Conversion and Energy Storage, Fujian Normal University, Fuzhou, Fujian 350117, P. R. China

Abstract Lead-free double perovskites (DPs) are emerging highly stable emitters with efficient broadband self-trapped exciton (STE) photoluminescence (PL), but their low electroluminescent (EL) efficiency is a critical shortcoming. We promoted the external quantum efficiency (EQE) and luminance of DP-based white light-emitting diode (wLED) with a normal device structure to 0.76% and 2793 cd m^{-2} via two modifications: We prevented the formation of adverse metallic silver, spatially confined STE, and lowered local site symmetry in $Cs_2Na_{0.4}Ag_{0.6}In_{0.97}Bi_{0.03}Cl_6$ DP by terbium doping; and we developed a

This article is protected by copyright. All rights reserved.

Accepted Article

guest-host strategy to improve film morphology, reduce defect density and increase carrier mobility. These alterations caused substantial increases in STE radiative recombination and charge injection efficiency of perovskite layer. Finally, pure white EL with ideal color coordinates of (0.328, 0.329) and a record-breaking optoelectronic performance was achieved by introducing additional green carbon dots in LED to fill the deficient green component.

Keywords lead-free double perovskites, light-emitting diodes, quantum dots, lanthanide dopants, self-trapped excitons.

Introduction

White LEDs have become one of major issues in the lighting and display industries, as LEDs possess superior efficiency and extended lifespan related to alternative technologies.[1-3] Currently, commercial wLEDs can be classified into two categories: optically excited devices utilizing blue LEDs with PL phosphors, and electrically excited devices based on red-green-blue (RGB) units.[4-8] Benefited from their size-tunable luminescent wavelengths and excellent solution processability, a unique type of emitters, quantum dots (QDs), as an

This article is protected by copyright. All rights reserved.

Accepted Article

alternative of traditional phosphors, have been commercially adopted as down-shifters for back-lighting in QDs liquid crystal displays (LCDs) to expand the achievable color gamut.[8-10] Over the past few years, EL of QDs provides another attractive route to exploit their superior emitting properties for the development of new-generation active-matrix QD LEDs (AM-QLEDs) displays.[11,12]

Recently, lead halide perovskite $APbX_3$ ($A=MA^+$, FA^+, Cs^+; $X=Cl^-$, Br^-, I^-) QDs have demonstrated their suitability as emitters of pure red, green, and blue light,[13-15] and white EL has been realized based on solution-processed hetero-phase halide perovskites that, unlike GaN-based wLEDs, feature a single broadband emissive layer without the need for phosphors.[6, 8] However, the usage of toxic heavy metal lead and intrinsic instability of $APbX_3$ still hamper the commercial application of perovskite QLEDs.[16,17] To address these concerns, researchers have turned their attention to DPs that yield broadband emission covering the whole visible spectrum via STE recombination.[18-21] However, no extensive studies on their EL devices have been carried out (**Table 1**). For example, Tang et al. pioneered the development of EL warm-white devices with a maximum luminance of 50 cd m^{-2} based on thermally evaporated $Cs_2Na_{0.4}Ag_{0.6}InCl_6$ microcrystals (MCs) film with trace Bi^{3+} doping;[18] Qu et al. successfully fabricated $Cs_2AgIn_{0.9}Bi_{0.1}Cl_6$ QDs wLEDs with a promoted luminance of 158 cd m^{-2} and EQE of 0.08% by triphenylphosphine oxide passivation;[22] Chen et al. demonstrated the first solution-processed EL devices using the

This article is protected by copyright. All rights reserved.

Accepted Article

$Cs_2AgIn_{0.9}Bi_{0.1}Cl_6$ DP nanoplatelets (NPLs) as the sole emitting component, showing a maximum luminance of 58 cd m^{-2} and EQE of 0.01%.[23] Despite these rapid progresses, realizing efficient broadband white EL based on STE recombination of DP remains challenging owing to low PLQYs, high-content defect states, high non-radiative transition probabilities, and poor charge mobilities within DP.

Here, a solution-processed Tb^{3+}-doped $Cs_2Na_{0.4}Ag_{0.6}In_{0.97}Bi_{0.03}Cl_6$ DP (TDP) film is prepared to act as a unique emitter with both efficient injection and recombination of carriers for DP wLEDs. A record luminance of 2793 cd m^{-2} and external quantum efficiency (EQE) of 0.76% are achieved via a guest-host strategy for the first time, which uses 4,4'-cyclohexylidenebis[N,N-bis(p-tolyl)aniline (TAPC) and 2,6-bis(3-(9H-carbazol-9-yl)phenyl)pyridine (2,6-DCzPPY) as TDP hosts. Structural/spectroscopic characterizations and first-principles density functional theory (DFT) calculations evidence that Tb^{3+} dopants effectively inhibit the formation of adverse metallic Ag nanoparticles, confine spatial distribution of STEs, and disrupt local site symmetry, ultimately leading to enhanced STE radiative recombination in TDP. Furthermore, the introduction of TAPC and 2,6-DCZPPY as host materials can significantly improve film morphology, reduce defect density and enhance carrier mobility. To our knowledge, this is the first report that the Ln^{3+} doped DPs used as the emitting layer in EL devices. More encouragingly, the wLED based on the combination of TDP/host and green carbon dots (G-CDs) as the emitting layer produces pure white

This article is protected by copyright. All rights reserved.

Accepted Article

luminescence with color coordinates of (0.328, 0.329), high color rendering index (CRI) of 87.7, correlated color temperature (CCT) of 5702 K, EQE of 0.695%, and luminance of 3163 cd m^{-2}, which substantially surpass those of recently reported lead-free DP-based wLEDs (**Table 1**). The research of this work will provide new insights into the design of Ln^{3+}-doped lead-free perovskites for lighting and display applications.

Table 1. Summary of optoelectronic performance of lead-free DP based LEDs reported so far. V_{on}, CE and L represent turn-on voltage, current efficiency and luminance.

Year	Material	V_{on} (V)	CE_{max} (cd A^{-1})	EQE_{max} (%)	L_{max} (cd m^{-2})	Ln^{3+}-doped	Ref.
2018	$Cs_2(Ag_{0.6}Na_{0.4})InCl_6$ MCs	8.4	0.110	/	50	No	[18]
2022	$Cs_2AgIn_{0.9}Bi_{0.1}Cl_6$ QDs	10.0	0.058	0.08	158	No	[22]
2023	2D-$Cs_2AgIn_{0.9}Bi_{0.1}Cl_6$ NPLs	5.5	0.013	0.01	58	No	[23]
2023	**DP**	**3.9**	**0.099**	**0.14**	**67.6**	**No**	**This work**
	DP/host	**3.3**	**0.153**	**0.43**	**1498**	**No**	
	TDP/host	**3.5**	**0.634**	**0.76**	**2793**	**Yes**	
	TDP/G-CDs/host	**3.1**	**1.157**	**0.70**	**3163**	**Yes**	

Results and Discussion

This article is protected by copyright. All rights reserved.

Accepted Article

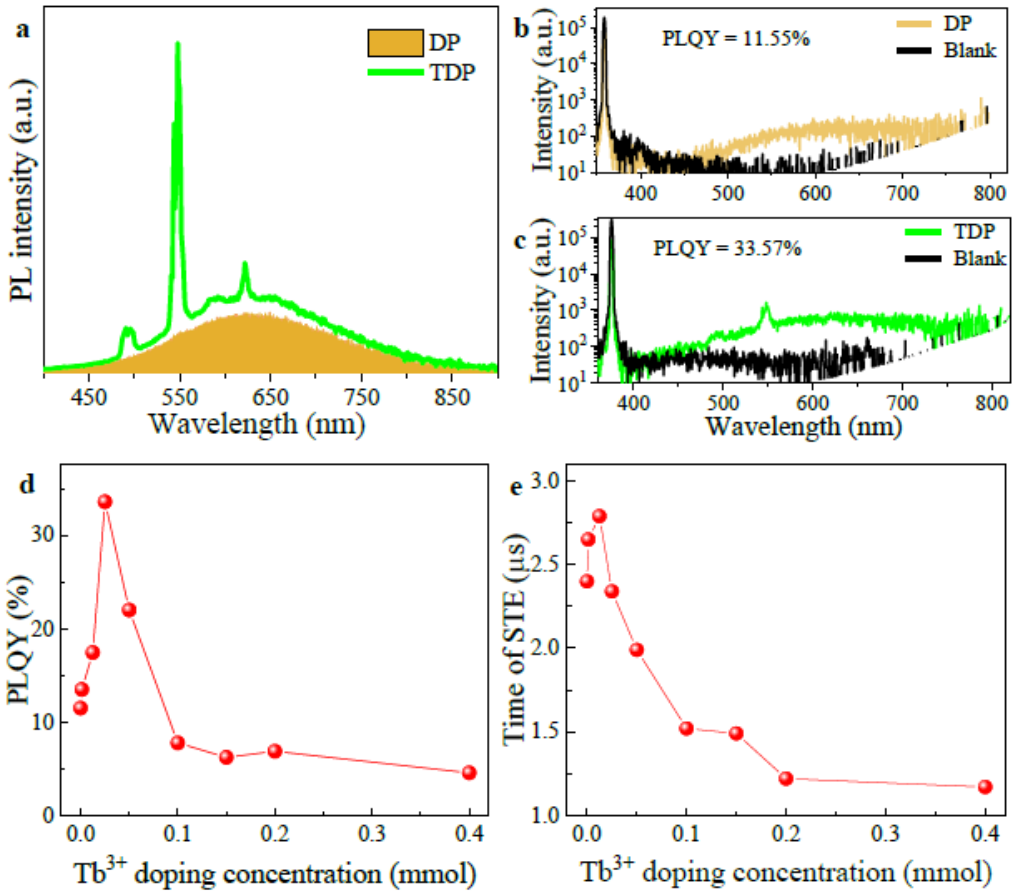

Figure 1. (**a**) PL spectra and (**b, c**) PLQYs of DP and TDP samples. (**d**) PLQY and (**e**) decay lifetime of STE versus Tb^{3+} doping concentrations.

A series of $Cs_2Na_{0.4}Ag_{0.6}In_{1-x}Bi_xCl_6$ DPs were synthesized by a modified hot-injection method (see **Methods**). The $Cs_2Na_{0.4}Ag_{0.6}In_{1-x}Bi_xCl_6$ (x=0~0.1) samples exhibit a typical broadband emission spanning the 400-950 nm range via the STEs recombination (**Figure 1a**), which stems from Jahn-Teller distortion of $[AgCl_6]^{5-}$ octahedra.[18] Importantly, trace amount

This article is protected by copyright. All rights reserved.

Accepted Article

of Bi^{3+} doping significantly enhances STE PL intensity, decay lifetime, and PLQY, as evidenced in **Figure S1**. Based on inductively coupled plasma-mass spectrometry (ICP-MS) analysis, the optimal Bi^{3+} doping concentration is determined to ~3 mol% corresponding to x=0.01 (**Table S1**), and PLQY of the DP sample is determined to be 11.55% (**Figure 1b**). Subsequently, Tb^{3+}-doped $Cs_2Na_{0.4}Ag_{0.6}In_{0.97}Bi_{0.03}Cl_6$ DPs were prepared, and the actual Tb^{3+} concentration can reach as high as ~27 mol% (**Table S1**). As shown in **Figure 1a**, besides broadband STE emission, several sharp PL bands around 492 nm ($^5D_4 \rightarrow {}^7F_6$), 548 nm ($^5D_4 \rightarrow {}^7F_5$), 585 nm ($^5D_4 \rightarrow {}^7F_4$), and 622 nm ($^5D_4 \rightarrow {}^7F_3$) ascribing to Tb^{3+} 4f-4f transitions are detected. Impressively, compared to DP sample, the PLQY of TDP is further promoted to 33.57% (**Figure 1c**, **Figure S2a**).

PL spectra of TDP with various Tb^{3+} doping contents are shown in **Figure S2b**. As the concentration of Tb^{3+} doping increases, the intensity of the Tb^{3+} emission gradually increases while the STE emission firstly enhances and then weakens. Temperature-depended PL spectra of both DP and TDP samples were recorded (**Figure S2c**, **S2d**) and the corresponding exciton binding energies were evaluated to be 76.71 meV for the DP and 80.23 meV for the TDP (**Figure S2e**, **S2f**). Therefore, it can be concluded that Tb^{3+}-doping leads to high exciton binding energy, which is beneficial for the enhancement of STE emission. The maximal STE emission is achieved for the 0.025 mmol Tb^{3+}-doped sample, and the similar variation trend is found for the results of PLQY (**Figure 1d**) and STE decay lifetime (**Figure 1e**). The

This article is protected by copyright. All rights reserved.

Accepted Article

optimal concentrations for the maximum PLQY and STE lifetime are 0.025 mmol and 0.0125 mmol, respectively. This difference is due to the occurrence of energy transfer from STE to Tb dopants. PL excitation (PLE) spectra corresponding to the broadband emission of STE at 650 nm are similar for both DP and TDP (**Figure S3**), and identical from those of the Tb^{3+} emissions at 492 nm, 548 nm, and 622 nm, indicating that these two emission centers arise from the relaxation of the same excited state. Time-resolved PL mapping of TDP QDs was measured in the range from 465 nm to 765 nm. The emission at 548 nm exhibits an ultra-long fluorescence lifetime decay within a time window of 38 ms (**Figure S4a**). However, when the time window is reduced to 19 μs, Tb^{3+} lifetime decay centered at 492 nm, 548 nm, 585 nm, and 622 nm, and a wide self-trapping lifetime decay can be observed (**Figure S4b**). The intensity within the time of the STE (650 nm) and Tb^{3+} (548 nm) emission centers was compared with the corresponding initial intensity, respectively. The results show that the decay rate of the STE PL intensity is very fast, while that of the Tb^{3+} is relatively slow (**Figure S4c**). The overall intensity is entirely contributed by Tb^{3+} PL after 6 μs, providing strong evidence that energy transfer (ET) occurred (**Figure S4d**). We collected the PL decay curves for the STE emission of DP and TDP. The decay curves of Tb^{3+} emission exhibited a typical parity-forbidden transitions with a millisecond lifetime (**Figure S5a**), whereas the decay lifetime for STE emission was only a few microseconds (**Figure S5b**). This short decay lifetime of STE can be attributed to the strong Jahn-Teller distortion-induced electron-hole recombination.[18, 21] Indeed, the gradual shortened lifetime of STE emission is recorded

This article is protected by copyright. All rights reserved.

Accepted Article

with increase of Tb^{3+} concentration (**Figure S5b**), confirming the occurrence of ET process from STE to Tb^{3+} dopants in TDP samples (**Figure S5c**). Furthermore, Tb^{3+}-alloying improves the PLQY compared with DP (**Table S2**). It is worth noting that the optimal PLQY (33.57%) of TDP is about 4-fold higher than the previously reported Bi^{3+}-doped $Cs_2Ag(In_{82.9\%}Tb_{17.1\%})Cl_6$ nanocrystals (NCs).[24]

This article is protected by copyright. All rights reserved.

Accepted Article

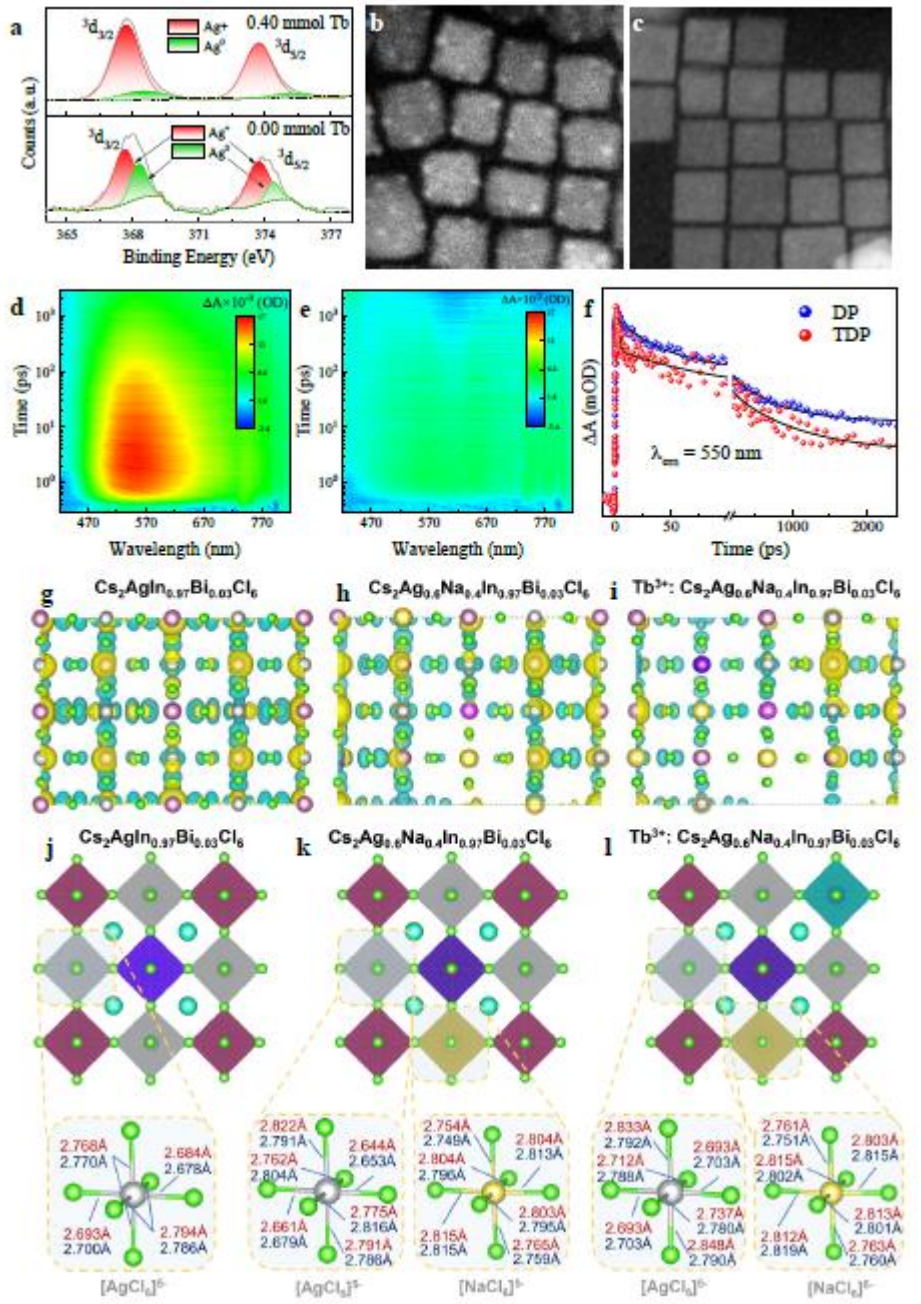

Figure 2. (**a**) High-resolution XPS spectra of Ag 3d measured for the DP and TDP QDs. HAADF-STEM images of (**b**) DP and (**c**) TDP samples. Pseudo-color fs-TA contour plots of the (**d**) DP and (**e**) TDP after excitation at 360 nm. (**f**) PIA decay dynamics for the samples probed at 550 nm. (**g-i**) STE and (**j-l**) schematic diagrams of sublattice distortion in

This article is protected by copyright. All rights reserved.

Accepted Article

$Cs_2AgIn_{0.97}Bi_{0.03}Cl_6$, $Cs_2Ag_{0.6}Na_{0.4}In_{0.97}Bi_{0.03}Cl_6$, and Tb^{3+}: $Cs_2Ag_{0.6}Na_{0.4}In_{0.97}Bi_{0.03}Cl_6$ DPs. Red, gray, purple, yellow, and cyan octahedrons represent $[InCl_6]^{3-}$, $[AgCl_6]^{5-}$, $[BiCl_6]^{3-}$, $[NaCl_6]^{5-}$, and $[TbCl_6]^{3-}$, respectively. Blue and red color data represent the bond length in $[AgCl_6]^{5-}$ and $[NaCl_6]^{5-}$ octahedrons at the ground state and the excited state, respectively.

To elucidate the mechanism behind the enhanced PLQY via Tb^{3+} doping, we performed structural and spectral characterizations. X-ray diffraction (XRD) patterns (**Figure S6**) show that all the TDP products are assigned to cubic double perovskite structure (ICSD number 257115) without phase separation, and the diffraction peaks slightly shift to lower angles with increase of Tb^{3+} content owing to partial substation of In^{3+} ions (r = 0.80 Å, CN = 6) by Tb^{3+} dopants (r = 0.92 Å, CN = 6). Based on X-ray photoelectron spectroscopy (XPS) data, signal peaks for the typical Cs 3d, Na 1s, Ag 3d, In 3d, Cl 2p, and Bi 4f are observed, along with an additional Tb 3d peak detected in the 0.10 mmol and 0.40 mmol TDP QDs (**Figure S7, S8**). The binding energy of In 3d or Bi 4f peaks decreases upon the introduction of Tb^{3+} dopants (**Figure S8**), while that of Cs 3d, Na 1s, Ag 3d, and Cl 2p exhibits little variation. These results indicate that Tb^{3+} ions have been successfully incorporated into DP lattice to modify ligand environments. In the Ag 3d spectra (**Figure 2a**), two peaks are observed at ~367.9 and ~374.0 eV that correspond to Ag $3d_{3/2}$ and $3d_{5/2}$ levels, respectively. Each of these peaks can be deconvoluted into two components assigned to Ag^+ ions (367.6 eV, 373.7 eV) and metallic Ag (368.3 eV, 374.4 eV).[25-27] The intensities of peaks that represent metallic Ag

This article is protected by copyright. All rights reserved.

Accepted Article

significantly decrease after Tb^{3+} doping. This result confirms that the formation of metallic Ag is successfully suppressed by Tb^{3+} doping. Transmission electron microscopy (TEM) images evidence that both DP and TDP have similar cubic morphology (**Figure S9**), and the mean size increases from 9.8 nm to 13.6 nm (**Figure S10**). High-resolution TEM micrographs show that TDP QDs possess high crystallinity without obvious lattice defects and show clear lattice fringes with spacings of 0.37 nm and 0.26 nm, corresponding to (220) and (400) crystal planes (**Figure S11**). Energy-dispersive X-ray (EDX) mapping confirms the uniform distribution of all the elements of Cs, Na, Ag, In, Cl, Bi, and Tb, in the TDP QDs (**Figure S12**). Notably, for the DP sample, lots of Ag particles are observed in the high-angle annular dark-field scanning TEM (HAADF-STEM) image (**Figure 2b**). It is believed that oleyl amine used in the present reaction can undergo metal-ion-induced oxidation to nitriles and reduce Ag^{+} ions to Ag nanoparticles.[27,28] Importantly, Tb^{3+} doping can significantly suppress the reduction of Ag^{+} ions, and indeed, no obvious Ag particles are detected in the HAADF-STEM image for the TDP sample (**Figure 2c**).

To understand the charge-carrier dynamics of the STE and ET process involved in the photoexcitation of the DP and TDP QDs, we carried out femtosecond transient-absorption (fs-TA) measurements pumped using a 360 nm pulsed laser. Pseudo-color TA contour plots are shown in **Figure 2d, 2e**. In the detection range of 420 to 820 nm, a broad positive photoinduced absorption (PIA) signal is observed for both samples, which could serve as

This article is protected by copyright. All rights reserved.

Accepted Article

direct evidence for the formation of STEs,[29-32] indicating that both samples share similar photophysical processes. Further inspection of the dynamics trajectory in the PIA band reveals that the rise time of DP and TDP QDs were 0.8 ps and 1.0 ps, respectively (**Figure S13**). This ultrafast ascent process is closely related to the relaxation of hot carriers (HCs) from high-energy states to STE state, and the elongation of rise time induced by Tb^{3+} doping is due to the reduction of HC loss during cooling, contributing to the higher PLQY of TDP. In addition, as shown in **Figure 2f**, the PIA decay curves probed at 550 nm are compared between DP and TDP, and the results show that the TDP QDs exhibit significantly faster dynamic response, which indicates that there is the presence of additional non-radiative pathways in the relaxation process. The PIA decay signals can be well-fitted by a bi-exponential function for DP QDs and a triexponential function for TDP QDs, where the ultrafast process (τ_1) related to surface defects or trap states and slow component (τ_2) associated with the radiative recombination of the STEs through photon emission. It is found that the τ_1 shortens from 64.1 ps to 9.0 ps, and the probability (A_1) decreases from 27.5% to 3.2%, which means that Tb^{3+} doping reduces the defect states and enhances the radiative recombination of the system (**Table S3**). An extra component (τ_3) in TDP QDs is attributed to the Tb^{3+} sensitization through a non-radiative ET pathway from STE to Tb^{3+}. Indeed, the calculated contribution of radiation relaxation rate (1.4×10^5 s^{-1}) in TDP QDs is much larger than that of pristine DP QDs (4.8×10^4 s^{-1}) (**Table S4**). These results unambiguously demonstrate that Tb^{3+} doping promotes the radiative recombination process in the TDP QDs.

This article is protected by copyright. All rights reserved.

Accepted Article

DFT calculations were further performed to explore Tb-dopants-induced structural evolution of DP. The calculated electronic structure and projected density of states reveal that the valence band maximum (VBM) is predominantly composed of the Cl-3p and Ag-4d orbitals, and the conduction band minimum (CBM) is mainly dominated by Cl-3p and In-5s orbitals (**Figure S14**). It can be observed that Tb^{3+} dopants primarily contribute to the conduction band at higher energy levels rather than influencing the band edges. To investigate the role of Tb^{3+} dopants for the enhanced STE emission in an atomic scale, more charge-density and geometry optimization calculations are implemented. For $Cs_2AgIn_{0.97}Bi_{0.03}Cl_6$, the electrons are strongly confined in $[InCl_6]^{3-}$ octahedrons in full real-space, and the holes are localized around $[AgCl_6]^{5-}$ octahedrons, especially distributed in the surrounding Cl^- anions (**Figure 2g**). The introduced $[NaCl_6]^{5-}$ octahedrons will aggravate the local distortion of $[AgCl_6]^{5-}$ octahedrons and reduce the electronic dimensionality of the $Cs_2Ag_{0.6}Na_{0.4}In_{0.97}Bi_{0.03}Cl_6$ (**Figure 2h**). The new inclusion of $[TbCl_6]^{3-}$ octahedron via replacing $[InCl_6]^{3-}$ in Tb^{3+}: $Cs_2Ag_{0.6}Na_{0.4}In_{0.97}Bi_{0.03}Cl_6$ TDPs leads to a more confinement of the spatial distribution of the STE state (**Figure 2i**). This indeed enhances the overlap between the electron and hole orbitals and results in the easier formation of the trapped excitons. Further microstructural analysis shows that the introduction of Bi^{3+}, Na^+ and Tb^{3+} enhances the sublattice distortion exclusively in the $[AgCl_6]^{5-}$ and $[NaCl_6]^{5-}$ octahedrons, while the $[InCl_6]^{3-}$, $[BiCl_6]^{3-}$ and $[TbCl_6]^{3-}$ octahedrons maintain high local O_h site symmetry (**Table S5**). In the case of $Cs_2AgIn_{0.97}Bi_{0.03}Cl_6$ DPs, the inclusion of Bi^{3+} specially induces

This article is protected by copyright. All rights reserved.

Accepted Article

the distortion in its nearest neighboring $[AgCl_6]^{5-}$ octahedrons. This distortion is evident in the shorter bond lengths of Ag-Cl pointing towards Bi^{3+} (2.678 and 2.700 Å), which are significantly shorter than the average Ag-Cl (2.755 Å) bond length, as depicted in **Figure 2j**. When the STE state is formed, the lattice distortion of $[AgCl_6]^{5-}$ octahedrons is further exacerbated, while the local O_h symmetries of $[InCl_6]^{3-}$ and $[BiCl_6]^{3-}$ octahedrons remain undisturbed (**Figure 2j**). In $Cs_2Na_{0.4}Ag_{0.6}In_{0.97}Bi_{0.03}Cl_6$ and Tb^{3+}: $Cs_2Na_{0.4}Ag_{0.6}In_{0.97}Bi_{0.03}Cl_6$, the doping of Na^+ and Tb^{3+} leads to the disorganization in the Ag-Cl and Na-Cl bond lengths (**Figure 2k, 2l**), thus resulting in the breakdown of local site symmetry of $[AgCl_6]^{5-}$ and $[NaCl_6]^{5-}$ octahedrons. A significant reduction in the local O_h symmetry of $[AgCl_6]^{5-}$ and $[NaCl_6]^{5-}$ octahedrons in TDPs (**Figure 2l**) promotes the localization of electron and hole orbitals (**Figure 2i**) and facilitates the formation of STEs.

Based on the above discussion, we proposed a possible luminescence mechanism to explain Tb-dopants-induced enhanced STE emission (**Figure S15**). When the electrons are excited from VBM to CBM of the TDP QDs by ultraviolet light to form free excitons, which will quickly relax to the self-trapped states and emit broadband yellow light through STE recombination. Tb^{3+} dopants will inhibit the formation of metallic Ag nanoparticles (reduce defect states), confine the spatial distribution of the STE state, and lower local site symmetry, which will improve STE radiation recombination. On the other hand, STE will transfer energy to Tb^{3+} dopants, which leads to Tb^{3+} emissions and concurrent reduction of STE

This article is protected by copyright. All rights reserved.

Accepted Article

luminescence. Therefore, doping appropriate content of Tb^{3+} ions (~3 mol%) can effectively promote STE emission and improve PLQY, making these materials promising for applications in EL wLED.

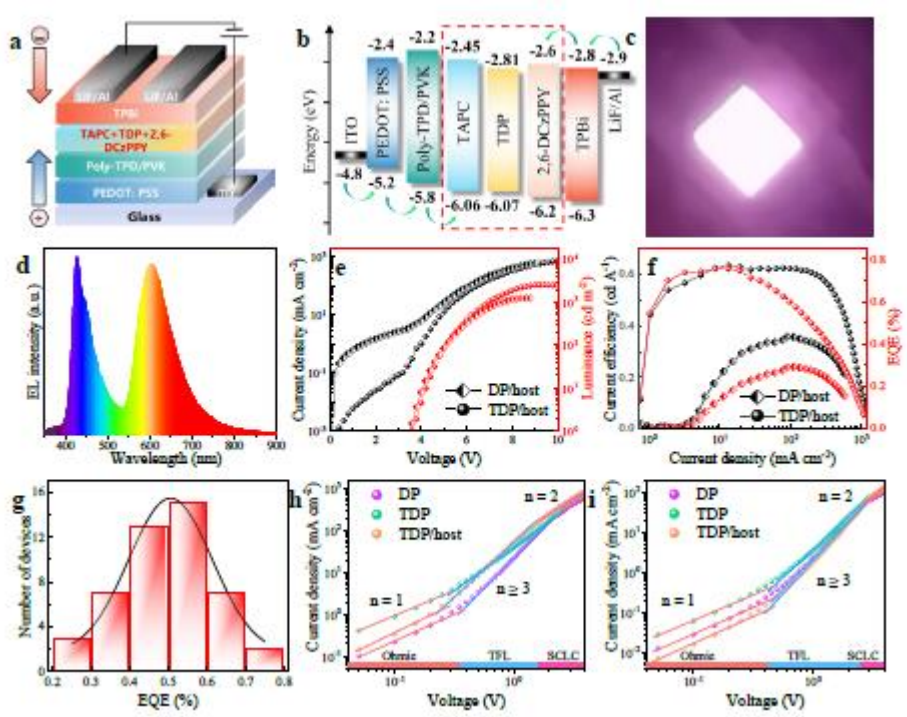

Figure 3. (**a**) Schematic illustration of wLED device structure. (**b**) Energy level diagram in the wLED device based on TDP QDs. (**c**) Photograph and (**d**) EL spectrum of the wLED under operation. (**e**) Current density-voltage-luminance and (**f**) current efficiency-current density-EQE characteristics of the wLED device based on DP/host and TDP/host, respectively. (**g**) Peak EQE histogram of wLED devices based on TPD/host. Current density versus voltage for (**h**) hole-only devices (V_{TFL} = 0.37 V (DP), 0.32 V (TDP), 0.24 V

This article is protected by copyright. All rights reserved.

Accepted Article

(TDP/host)), and (**i**) electron-only devices (V_{TFL} = 0.49 V (DP), 0.46 V (TDP), 0.42 V (TDP/host)). The SCLC region identified from the J-V curves are linearly fitted to estimate hole and electron mobilities in the respective thin films.

Furthermore, TDP QDs were subjected to a series of stability measurements. XRD patterns and steady-state PL spectra remain unaltered over four months of exposure to air (**Figure S16a, S16b**), suggesting excellent structural and optical stability. Thermogravimetric (TG) curve shows that the QDs exhibit no significant thermal decomposition from room temperature to 502 °C (**Figure S16c**). Meanwhile, TDP QDs display excellent thermal stability without an observable change in PL intensity after three heating cycles, and the luminescence intensity of the sample at 420 K maintained 82% of that at 100 K (**Figure S16d**).

To adopt DP and TDP as the emitting layers for fabricating LEDs, we prepared DP and TDP films and their PL performance was investigated. No obvious PL degradation for the films is found owing to super stability of DP/TDP QDs (**Figure S17**), which is quite different to the case of lead halide perovskites.[33-35] The DP/TDP based wLED device structure of ITO/PEDOT: PSS/Poly-TPD/PVK/TAPC + DP/TDP + 2,6-DCzPPY (55 nm)/TPBi (40 nm)/LiF (1 nm)/Al (100 nm) is schematically illustrated in **Figure 3a**. Here, ITO, PEDOT: PSS, Poly-TPD/PVK, TPBi, and LiF/Al are utilized as anode, hole-injection layer, hole transporting layer, electron transporting layer, and cathode, respectively. These functional

This article is protected by copyright. All rights reserved.

Accepted Article

layers can be clearly discerned from cross-sectional scanning electron microscopy (SEM) image of the device (**Figure S18**). As is well known, obtaining high-quality film with QDs dispersed is crucial for fabricating EL devices. To this end, we collected the film micromorphology of the QDs through SEM and observed some apparent holes and rough surfaces on the film of neat TDP QDs (**Figure S19a**). Notably, introducing organic host materials of TAPC and 2,6-DCzPPY into the emitting layer, the film morphology exhibited more uniform, dense, and almost void-free since the organic molecules, possessing better dispersion, can well fill the gaps among the QDs (**Figure S19b, S19c**). The highest occupied molecular orbitals (HOMO) and lowest unoccupied molecular orbitals (LUMO) of TAPC, DP, and TDP were determined by ultraviolet photoelectron spectroscopy (UPS), and their corresponding HOMO/LUMO values are 6.06/2.45 eV, 6.09/2.83 eV, and 6.07/2.81 eV, respectively (**Figure S20**). The energy levels of the remaining layers are taken from references (**Figure 3b**).[36] In short, this effective energy level matching can enhance carrier injection efficiency, improve carrier transport rate, optimize electron-hole recombination processes, and enhance the stability and long-term performance of the devices.[22,23,37,38] These advantages have significant impacts on the performance and efficiency of wLED devices.

Upon operation, the device shows bright white electroluminescence with dual-emitting bands located at 430 nm and 610 nm (**Figure 3c, 3d**). The recorded EL spectra show no obvious change with increase of bias voltage (**Figure S21a**). In addition, the device with the

This article is protected by copyright. All rights reserved.

Accepted Article

similar structure without perovskite layer has been designed (**Figure S21b**). The recorded EL spectra show no DP emission, excluding the influence of interface interaction or exciplex (**Figure S21c**). According to the normalized PL spectra of Poly-TPD, PVK, TAPC, 2,6-DCzPPY, and DP QDs, it can be concluded that the low-energy band emission comes from STE recombination of DP QDs, while the high-energy band originates from the contribution of Poly-TPD (**Figure S22**). Herein, the EL spectrum shows a little blue shift compared with PL spectrum, which has also been observed in previously reported lead-free DP based EL spectra.[22] This may be attributed to several influencing factors such as excitation mechanism, energy level structure, lattice effect, surface effect, temperature effect and inhomogeneity/defect. Notably, different to PL spectra, Tb^{3+} emissions are absent in the EL spectra of TDP-based device, which can be attributed to parity-forbidden 4f-4f transitions and low radiative transition rate of Tb^{3+} ions.[39] The current density-voltage-luminance characteristics and current efficiency-current density-EQE curves of the devices are shown in **Figure 3e, 3f** and **Figure S23**. The maximum luminance and EQE of the DP-only LED are only 67.6 cd/m^2 and 0.14%, which are improved to 1498 cd m^{-2} and 0.43% after introducing TAPC and 2,6-DCzPPY as host. More importantly, the values can be further enhanced up to 2793 cd m^{-2} and 0.76% for the TDP/host-based device, which correspondingly increase by 48-fold and 76-fold compared with those of 58 cd m^{-2} and 0.01% for the two-dimensional $Cs_2AgIn_{0.9}Bi_{0.1}Cl_6$ NPLs based LED (**Table 1**). As shown in **Figure 3g**, the average peak EQE of the TDP device is 0.51%, with a small standard deviation. In addition, the turn-on

This article is protected by copyright. All rights reserved.

Accepted Article

voltage of 3.5 V is much lower than the 8~10 V reported in previous work. As tabulated in **Table 1**, all the reported DP-based wLEDs are the normal device structure. Compared with the previously reported ones, the present TDP-based wLED exhibits substantial improvement in CE from 0.110 cd A^{-1} to 0.634 cd A^{-1}, EQE from 0.08% to 0.76%, and luminance from 158 cd m^{-2} to 2793 cd m^{-2}, benefited from terbium doping and the designed guest-host strategy. However, compared with lead halide perovskites based EL devices, its performance is still far from satisfactory. Further researches should concentrate on the improvement of PLQY and charge injection efficiency, and reduction of defects in DP emitting layer.

Table 2. Summary of defect densities and carrier mobilities of the films based on DP, TDP, and TDP/host. N_{th}, N_{te}, μ_h, and μ_e represent hole-defect density, electron-defect density, hole mobility, and electron mobility, respectively.

Material	**DP**	**TDP**	**TDP/host**
N_{th} **(cm^{-3})**	3.73×10^{16}	3.23×10^{16}	2.42×10^{16}
N_{te} **(cm^{-3})**	4.94×10^{16}	4.64×10^{16}	4.23×10^{16}
μ_h **(cm^2 V^{-1}s^{-1})**	2.02×10^{-2}	2.74×10^{-2}	2.98×10^{-2}
μ_e **(cm^2 V^{-1}s^{-1})**	3.56×10^{-3}	4.10×10^{-3}	6.50×10^{-3}

This article is protected by copyright. All rights reserved.

Accepted Article

To illustrate enhancement mechanism of device performance based on the emitting layer of TDP/host, single-carrier devices were fabricated to determine defect density and carrier mobility. The hole-only and electron-only devices with configurations of ITO/PEDOT: PSS/QDs/MoO_3/Ag and ITO/ZnO/QDs/TPBi/LiF/Al were designed. As shown in **Figure 3h**, **3i**, the current density-voltage curves display three different slopes ascribing to a linear ohmic region ($I \propto V^{n=1}$), trap-filled limit (TFL) region ($I \propto V^{n\geq 3}$), and quadratic space charge limit current (SCLC) region ($I \propto V^{n=2}$). The corresponding defect density (N_t) can be obtained by the following equation:[40]

$$N_t = \frac{2\varepsilon_0 \varepsilon V_{TFL}}{eL^2} \quad (1)$$

where V_{TFL} is the TFL voltage (kink point from ohmic to trap-filled region), L is the thickness of the emission layer (55 nm), ε_0 and ε are the vacuum permittivity and the relative dielectric constant (ε = 2.76).[41,42] The calculated hole(electron)-defect densities of DP, TDP, and TDP/host films are 3.73×10^{16} (4.94×10^{16}), 3.23×10^{16} (4.64×10^{16}), and 2.42×10^{16} cm^{-3} (4.23×10^{16}), respectively (**Table 2**), illustrating that the introduction of Tb^{3+} ions and the organic molecule can effectively passivate the defects. Then, the carrier mobility (μ_h and μ_e, which the subscripts "e" and "h" represent holes and electrons, respectively) can be estimated according to the equation[35]

$$\mu = \frac{8JL^3}{9\varepsilon_0 \varepsilon V^2} \quad (2)$$

This article is protected by copyright. All rights reserved.

Accepted Article

where J and V are the current density and the applied voltage, respectively. The plots of J-V^2 are shown in **Figure S24** and the calculated hole and electron mobilities are tabulated in **Table 2**. Apparently, the carrier mobilities of the DP, TDP, and TDP/host experience a significant enhancement, and the hole and electron mobilities of TDP/host reach 2.98×10^{-2} and 6.50×10^{-3} cm^2 V^{-1} s^{-1}, respectively. These suggest that the introduction of Tb^{3+} dopants and TAPC/2,6-DCzPPY host is beneficial to reduce defect density and improve charge injection efficiency in LED device.

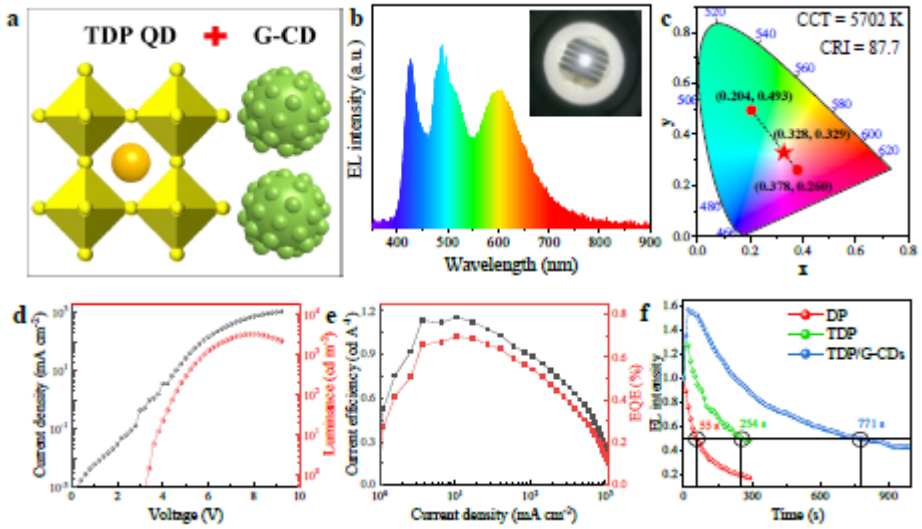

Figure 4. (**a**) Schematic diagram of the mixture of TPD QDs and G-CDs. (**b**) EL spectrum of the TDP/G-CDs/host-based wLED. Inset: photograph of the wLED under operation. (**c**) CIE color coordinates for the wLED. (**d**) Current density-voltage-luminance and (**e**) current

This article is protected by copyright. All rights reserved.

Accepted Article

efficiency-current density-EQE characteristics of the wLED device. (**f**) Operating stabilities of the DP-, TDP- and TDP/G-CDs-based LED devices after applying the voltage at 5.0 V.

In order to obtain a pure white light closer to (0.33, 0.33) of Commission Internationale de l'Eclairage (CIE) color coordinates, we introduced additional green-carbon dots (G-CDs) to fill the missing green component (**Figure 4a**). PL spectrum shows a green emission at 495 nm for the G-CDs and its PLQY reaches as high as 91.95% (**Figure S25**). Importantly, adjusting the ratio of TDP to G-CDs (TDP:G-CDs = 3:1, 7:1, 14:1, 21:1, 28:1) in the emitting layer can finally realize white light emission for the TDP/G-CDs/host-based LED devices (**Figure S26a**). A typical EL spectrum and digital photograph of the wLED device (TDP:G-CDs = 21:1) are shown in **Figure 4b**. The CIE color coordinates of the wLED output is (0.328, 0.329) with a correlated color temperature (CCT) of 5702 K and a color rendering index (CRI) of 87.7 (**Figure 4c**). Meanwhile, when the ratio of TDP:G-CDs is reduced to 3:1, the LED device at 6 V yields green light with color coordinates of (0.276, 0.425) (**Figure S27**). Notably, the color coordinates of the TDP/host (0.378, 0.260), TDP/G-CDs/host (0.328, 0.329), and G-CDs/host (0.204,0.493) based LED are found to lie along a straight line in the CIE diagram, verifying highly tunable EL colors for the constructed wLEDs. The current density-voltage-luminance characteristics and current efficiency-current density-EQE curves of TDP/G-CDs/host devices are shown in **Figure 4d, 4e** and **Figure S26b, S26c**. The best-performing wLED device based on TDP/G-CDs/host exhibits turn-on voltage of 3.1 V, current efficiency of 1.157 cd A^{-1}, EQE of 0.70%, and luminance up to 3163 cd m^{-2} (**Table S6**), which far exceed those of recently reported lead-free DP based wLEDs (**Table 1**).

This article is protected by copyright. All rights reserved.

Accepted Article

Finally, the operation stability of the device was monitored by applying a constant voltage at 5.0 V. As depicted in **Figure 4f**, the T_{50} lifetimes of wLED based on DP/host, TDP/host, and TDP/G-CDs/host are evaluated to be 55 s, 254 s, 771 s, respectively. The results further verify the effectiveness of using Tb dopants and guest-host strategy in EL devices. Overall, the optoelectronic performance of the as-prepared TDP/host and TDP/G-CDs/host based wLEDs in this study is superior to that of their counterparts, particularly for the key parameters of white-emitting luminance and EQE.

Conclusion

We demonstrate that appropriate amount of Tb^{3+} dopants can substantially improve PLQY of $Cs_2Na_{0.4}Ag_{0.6}In_{0.97}Bi_{0.03}Cl_6$ lead-free DP from ~11.55% to ~33.57%. A series of structural characterizations, steady/transient-state PL spectra, fs-TA spectra and DFT calculations verify that such enhanced STE radiative recombination is attributed to the inhibited formation of metallic Ag nanoparticles, the confined spatial distribution of STEs, and the reduction of local site symmetry after Tb^{3+} doping. The as-prepared TDP is adopted as the emitting layer to construct the wLED with a normal structure via a guest-host strategy for the first time, where TAPC and 2,6-DCzPPY organic materials are utilized as TDP host to improve film morphology, reduce defect density and increase carrier mobility. As a consequence, a record luminance of 2793 cd m^{-2} and EQE of 0.76% are achieved, far

This article is protected by copyright. All rights reserved.

Accepted Article

exceeding those of recently reported lead-free DP based wLEDs. Finally, the wLED based on the combination of TDP/host and G-CDs as the emitting layer is designed to produce pure white light with CIE color coordinates close to (0.33, 0.33), high CRI of 87.7, CCT of 5702 K, EQE of 0.70%, and luminance of 3163 cd m^{-2}. This research opens the door to electrically driven single-emissive-layer wLEDs based on solution-processed and stable lanthanide-doped lead-free double perovskites, which merits further study to realize their full potential for display and lighting applications.

Supporting Information

Supporting Information is available from the Wiley Online Library or from the author.

Corresponding Author

E-Mail: dqchen@fjnu.edu.cn (D. Q. Chen)

This article is protected by copyright. All rights reserved.

Accepted Article

Declaration of Competing Interest

The authors declare no competing financial interests.

Acknowledgements

This research was financially supported by the National Key Research and Development Program of China (2021YFB3500503), National Natural Science Foundation of China (52272141, 51972060, 12074068, 52102159 and 22103012), Natural Science Foundation of Fujian Province (020J02017, 2022J05091, 22021J06021, 2021J01190 and 2020J01931) and Fujian Science & Technology Innovation Laboratory for Optoelectronic Information (2021ZZ126).

References

[1] Y. H. Hwang, B. Noh, J. Lee, H. S. Lee, Y. Park, K. C. Choi, *Adv. Sci.* **2022**, *9*, 2104855.

[2] P. Dang, G. Li, X. Yun, Q. Zhang, D. Liu, H. Lian, M. Shang, J. Lin, *Light. Sci. Appl.* **2021**, *10*, 29.

[3] J. Chen, S. Mukherjee, W. Li, H. Zeng, R. A. Fischer, *Nat. Rev. Mater.* **2022**, *7*, 677.

This article is protected by copyright. All rights reserved.

Accepted Article

[4] P. Pust, V. Weiler, C. Hecht, A. Tucks, A. S. Wochnik, A. K. Henss, D. Wiechert, C. Scheu, P. J. Schmidt, W. Schnick, *Nat. Mater.* **2014**, *13*, 891.

[5] G. Li, Y. Tian, Y. Zhao, J. Lin, *Chem. Soc. Rev.* **2015**, *44*, 8688.

[6] Z. Chen, Z. Li, Z. Chen, R. Xia, G. Zou, L. Chu, S.-J. Su, J. Peng, H.-L. Yip, Y. Cao, *Joule* **2021**, *5*, 456.

[7] J. Chen, J. Wang, X. Xu, J. Li, J. Song, S. Lan, S. Liu, B. Cai, B. Han, J. T. Precht, D. Ginger, H. Zeng, *Nat. Photonics* **2020**, *15*, 238.

[8] R. Wang, H. Xiang, Y. Li, Y. Zhou, Q. Shan, Y. Su, Z. Li, Y. Wang, H. Zeng, *Adv. Funct. Mater.* **2023**, *33*, 2215189.

[9] A. R. Anwar, M. T. Sajjad, M. A. Johar, C. A. Hernández-Gutiérrez, M. Usman, S. P. Łepkowski, *Laser Photonics Rev.* **2022**, *16*, 2100427.

[10] J. Lin, Y. Lu, X. Li, F. Huang, C. Yang, M. Liu, N. Jiang, D. Chen, *ACS Energy Lett.* **2021**, *6*, 519.

[11] R. Wang, H. Xiang, J. Chen, Y. Li, Y. Zhou, W. C. Choy, Z. Fan, H. Zeng, *ACS Energy Lett.* **2022**, *7*, 2173.

[12] L. Xu, J. Li, B. Cai, J. Song, F. Zhang, T. Fang, H. Zeng, *Nat. Commun.* **2020**, *11*, 3902.

[13] J. Jiang, Z. Chu, Z. Yin, J. Li, Y. Yang, J. Chen, J. Wu, J. You, X. Zhang, *Adv. Mater.* **2022**, *34*, 2204460.

[14] C. Sun, Y. Jiang, M. Cui, L. Qiao, J. Wei, Y. Huang, L. Zhang, T. He, S. Li, H. Y. Hsu, C. Qin, R. Long, M. Yuan, *Nat. Commun.* **2021**, *12*, 2207.

[15] W. Zhou, Y. Shen, L. X. Cao, Y. Lu, Y. Y. Tang, K. Zhang, H. Ren, F. M. Xie, Y. Q. Li, J. X. Tang, *Adv. Funct. Mater.* **2023**, *33*, 2301425.

[16] P. Docampo, T. Bein, *Acc. Chem. Res.* **2016**, *49*, 339.

[17] A. Babayigit, A. Ethirajan, M. Muller, B. Conings, *Nat. Mater.* **2016**, *15*, 247.

[18] J. Luo, X. Wang, S. Li, J. Liu, Y. Guo, G. Niu, L. Yao, Y. Fu, L. Gao, Q. Dong, C. Zhao, M. Leng, F. Ma, W. Liang, L. Wang, S. Jin, J. Han, L. Zhang, J. Etheridge, J. Wang, Y. Yan, E. H. Sargent, J. Tang, *Nature* **2018**, *563*, 541.

This article is protected by copyright. All rights reserved.

Accepted Article

[19] B. Zhou, Z. Liu, S. Fang, H. Zhong, B. Tian, Y. Wang, H. Li, H. Hu, Y. Shi, *ACS Energy Lett.* **2021**, *6*, 3343.

[20] P. Zhu, S. Thapa, H. Zhu, S. Wheat, Y. Yue, D Venugopal, *J. Alloy. Compd.* **2023**, *960*, 170836.

[21] G. Zhang, D. Wang, B. Lou, C. G. Ma, A. Meijerink, Y. Wang, *Angew. Chem. Int. Ed.* **2022**, *61*, e202207454.

[22] Y. Zhang, Z. Zhang, W. Yu, Y. He, Z. Chen, L. Xiao, J. J. Shi, X. Guo, S. Wang, B. Qu, *Adv. Sci.* **2022**, *9*, 2102895.

[23] Z. Liu, Y. Sun, T. Cai, H. Yang, J. Zhao, T. Yin, C. Hao, M. Chen, W. Shi, X. Li, L. Guan, X. Li, X. Wang, A. Tang, O. Chen, *Adv. Mater.* **2023**, *35*, 2211235.

[24] Y. Liu, X. Rong, M. Li, M. S. Molokeev, J. Zhao, Z. Xia, *Angew. Chem. Int. Ed.* **2020**, *59*, 11634.

[25] Y. Liu, Y. Jing, J. Zhao, Q. Liu, Z. Xia, *Chem. Mater.* **2019**, *31*, 3333.

[26] S. Levy, S. Khalfin, N. G. Pavlopoulos, Y. Kauffmann, G. Atiya, S. Shaek, S. Dror, R. Shechter, Y. Bekenstein, *Chem. Mater.* **2021**, *33*, 2370.

[27] Z. Liu, J. Zito, M. Ghini, L. Goldoni, M. Prato, H. Bahmani Jalali, I. Infante, L. De Trizio, L. Manna, *Nano Lett.* **2022**, *22*, 8567.

[28] Y. Bekenstein, J. C. Dahl, J. Huang, W. T. Osowiecki, J. K. Swabeck, E. M. Chan, P. Yang, A. P. Alivisatos, *Nano Lett.* **2018**, *18*, 3502.

[29] B. Yang, X. Mao, F. Hong, W. Meng, Y. Tang, X. Xia, S. Yang, W. Deng, K. Han, *J. Am. Chem. Soc.* **2018**, *140*, 17001.

[30] M. Cong, B. Yang, F. Hong, T. Zheng, Y. Sang, J. Guo, S. Yang, K. Han, *Sci. Bull.* **2020**, *65*, 1078.

[31] P. Han, C. Luo, S. Yang, Y. Yang, W. Deng, K. Han, *Angew. Chem. Int. Ed.* **2020**, *59*, 12709.

[32] X. Cheng, Z. Xie, W. Zheng, R. Li, Z. Deng, D. Tu, X. Shang, J. Xu, Z. Gong, X. Li, X. Chen, *Adv. Sci.* **2022**, *9*, 2103724.

[33] J. Song, T. Fang, J. Li, L. Xu, F. Zhang, B. Han, Q. Shan, H. Zeng, *Adv. Mater.* **2018**, *30*, e1805409.

This article is protected by copyright. All rights reserved.

Accepted Article

[34] R. Sun, P. Lu, D. Zhou, W. Xu, N. Ding, H. Shao, Y. Zhang, D. Li, N. Wang, X. Zhuang, B. Dong, X. Bai, H. Song, *ACS Energy Lett.* **2020**, *5*, 2131.

[35] R. Sun, D. Zhou, Y. Ding, Y. Wang, Y. Wang, X. Zhuang, S. Liu, N. Ding, T. Wang, W. Xu, H. Song, *Light: Sci. Appl.* **2022**, *11*, 340.

[36] J. L. Li, Y. F. Sang, L. J. Xu, H. Y. Lu, J. Y. Wang, Z. N. Chen, *Angew. Chem. Int. Ed.* **2022**, *61*, e202113450.

[37] T. Bai, X. Wang, Z. Wang, S. Ji, X. Meng, Q. Wang, R. Zhang, P. Han, K. L. Han, J. Chen, F. Liu, B. Yang, *Angew. Chem. Int. Ed.* **2023**, *62*, e202213240.

[38] Z. Ma, X. Ji, M. Wang, F. Zhang, Z. Liu, D. Yang, M. Jia, X. Chen, D. Wu, Y. Zhang, X. Li, Z. Shi, C. Shan, *Adv. Sci.* **2022**, *9*, e2202408.

[39] G. Pan, X. Bai, D. Yang, X. Chen, P. Jing, S. Qu, L. Zhang, D. Zhou, J. Zhu, W. Xu, B. Dong, H. Song, *Nano Lett.* **2017**, *17*, 8005.

[40] Y. F. Qingfeng Dong, Yuchuan Shao, Padhraic Mulligan, Jie Qiu, Lei Cao, Jinsong Huang, *Science* **2015**, *347*, 967.

[41] C. J. Yu, I. C. Ri, H. M. Ri, J. H. Jang, Y. S. Kim, U. G. Jong, *RSC Adv.* **2023**, *13*, 16012.

[42] W. Pan, H. Wu, J. Luo, Z. Deng, C. Ge, C. Chen, X. Jiang, W.-J. Yin, G. Niu, L. Zhu, L. Yin, Y. Zhou, Q. Xie, X. Ke, M. Sui, J. Tang, *Nat. Photonics* **2017**, *11*, 726.

Terbium doping and guest-host strategy are adopted to substantially enhance self-trapped exciton radiative recombination and charge injection efficiency in lead-free DP emitting layer. Consequently, a record luminance of 2793 cd m^{-2} and external quantum efficiency of 0.76% for the constructed white LED are reported, substantially surpassing those of recently reported DP based EL devices.

This article is protected by copyright. All rights reserved.

Accepted Article

Authors Shilin Jin, He Yuan, Tao Pang, Manjia Zhang, Junyang Li, Yuanhui Zheng, Tianmin Wu, Ruidan Zhang, Zhibin Wang, Daqin Chen

Title Highly bright and stable lead-free double perovskite white light-emitting diodes

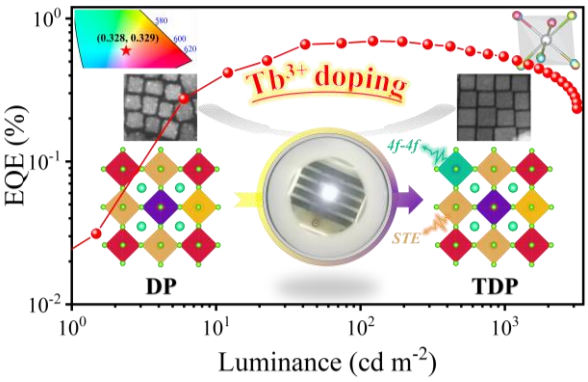

This article is protected by copyright. All rights reserved.